Journal of Materials Science: Materials in Electronics (2019) 30:16676–16686
https://doi.org/10.1007/s10854-019-02048-8

Investigation of the temperature-dependent electrical properties of Au/PEDOT:WO_3/p-Si hybrid device

Mine Keskin[1] · Abdullah Akkaya[2] · Enise Ayyıldız[3] · Ayşegül Uygun Öksüz[4] · Mücella Özbay Karakuş[5]

Received: 8 April 2019 / Accepted: 16 August 2019 / Published online: 24 August 2019

Abstract

The electrical properties of Au/PEDOT:WO_3/p-Si hybrid devices were studied in terms of current–voltage *(I–V)* and capacitance–voltage *(C–V)* measurements. Poly (3,4-ethylene dioxythiophene/tungsten trioxide (PEDOT:WO_3) composite was prepared by an in situ chemical oxidative polymerization of monomer in 1-butyl-3-methylimidazoliumtetrafluoroborate (BMIMBF4). Optical and structural properties of the PEDOT:WO_3 thin film was characterized by using FTIR, UV–Vis and AFM techniques. The bandgap energy of PEDOT:WO_3 thin film was determined as 2.07 eV from UV–Vis spectrum. It was seen that the *I–V* plots of the Au/PEDOT:WO_3/p-Si hybrid devices were non-linear and C^{-2}–*V* plots were linear in the reverse bias defining rectification behavior. The values of barrier height obtained from the *I–V* and C^{-2}–*V* plots of the fabricated devices were found to be 0.729 ± 0.012 eV and 0.817 ± 0.011 eV at room temperature in the dark environment, respectively. Devices have a high rectification behavior with a rectification ratio of 3.645×10^5 at ± 1 V. The temperature-dependent *I–V* characteristics of one of the devices were also analyzed on the basis of the thermionic emission theory at low forward bias voltage regime. It was observed that the values of ideality factor decrease while the values of barrier height increase with increasing temperature. This kind of temperature dependence was attributed to the presence of the barrier inhomogeneity at the hybrid film/inorganic semiconductor interface. Then, by analysing of the forward bias *I–V* characteristics at double logarithmic scale, it was seen that the carrier transport in the Au/PEDOT:WO_3/p-Si hybrid device demonstrates the space-charge-limited current (SCLC) conduction mechanism controlled by a trap distribution above the valence band edge dominates in the range 0.1–0.3 V voltages. Furthermore, by analyzing the reverse bias *I–V–T* characteristics, it was shown that Schottky emission was the dominating current conduction mechanism in the temperature range of 240–320 K.

1 Introduction

Efficient works are being done on the production of new materials which can be used in semiconductor technology. For this purpose, many chemical compounds have been explored and developed for the micro- and optoelectronic devices, such as conjugated polymers [1–8], Metallo-phthalocyanine (MPc) [9–11], metal oxides [12–15]. Polymeric and non-polymeric organic materials have attracted increasing interest because of their easy processing, potential low-cost applications, great opportunity to modify their excellent compatibility with a variety of substrates and chemical structures [1–6]. The device performance is controlled by arranging the charge conduction properties of organic semiconductors. It is generally accepted that doping in organic semiconductors or polymers can alter the carrier mobility. Li et al. [16] investigated the effects of scattering and trapping by dopant on the hole transport properties of N,N′-diphenyl-N,N′-bis(1-naphthyl)-1,1′-biphenyl-4,4′-diamine (NPB).

✉ Enise Ayyıldız
enise@erciyes.edu.tr

1 Department of Physics, Graduate School of Natural and Applied Sciences, Erciyes University, 38039 Kayseri, Turkey

2 Tech. Prog. Dept., Mucur Technical Vocational Schools, Ahi Evran University, 40500 Kırşehir, Turkey

3 Department of Physics, Faculty of Sciences, Erciyes University, 38039 Kayseri, Turkey

4 Department of Chemistry, Faculty of Arts and Sciences, Süleyman Demirel University, 32260 Isparta, Turkey

5 Department of Computer Engineering, Faculty of Engineering and Architecture, Bozok University, 66000 Yozgat, Turkey

The admittance spectroscopy, temperature-dependent current–voltage characteristics, and luminance-voltage characteristics were used to reveal the roles of trap and scatter played in NPB. They revealed that dopant molecules as trapping decreases the hole mobility and increases the density of traps whereas doping molecules as scattering then does not obviously affect the hole transport.

Poly(3,4-ethylene dioxythiophene) (PEDOT) is one of the most attractive materials among the variety of conducting polymers due to its great electrical properties, environmental stability and easy fabrication process [17, 18]. Tungsten trioxide (WO_3) is also one of the most exciting materials in transition metal oxides and, exhibiting a wide variety of novel properties, particularly in thin film form, useful for technological applications. WO_3 has many advantages, including excellent chemical stability, color switching, and strong adherence to the substrate [14]. WO_3 insertion in an inverted organic light emitting diode structure causes an interfacial energy level alignment of hole injection layers and its effects the electroluminescence properties [19]. It was shown that the current efficiency and electroluminescence properties of this structural device were greatly enhanced with WO_3 interlayer. Researchers noticed that many pristine materials like ceramics, plastics or metals could not complete the technological requirements for various new applications and found that the combination of some materials to form hybrids can show unexpected properties when compared with own original components. The primary motivation behind creating a hybrid material is to utilize the electrical, mechanical, thermal, and structural properties of the inorganic material and flexibility, functionality and template ability of the organic material [18].

In this study, poly(3,4-ethylene dioxythiophene)/tungsten trioxide (PEDOT:WO_3) composite using as an interfacial layer in between the Au and p-Si was prepared by an in situ chemical oxidative polymerization of monomer in 1-butyl-3-methylimidazoliumtetrafluoroborate. The chemically synthesized PEDOT:WO_3 was dissolved in *N*-methyl pyrrolidine, and then used to form thin interfacial layer by spin coating on to the chemically cleaned silicon substrate. The *I–V* and *C–V* measurements were used for characterizing the electrical properties of the Au/PEDOT:WO_3/p-Si devices. Particularly, the temperature dependence of the *I–V* characteristics was studied to obtain information about the conduction mechanisms of the devices.

2 Experimental procedures

In the fabrication procedure of the hybrid devices, p-type Si wafer with (100) orientation, one-sided polished, 500–550 μm thickness and 0.06–0.2 Ωcm resistivity was used. The wafer was cleaned using the RCA procedure [20]. The Ohmic contact was made by evaporating Au–Sb (99%, 1%) alloy on the back surface of the p-Si substrate. The evaporated film thickness was monitored using a quartz oscillator (QCM) and the metal film had a thickness of 50 nm. The contact was annealed at 450 °C for 3 min in flowing high purity (5 N) argon gas in the quartz tube furnace. Poly(3,4-ethylenedioxythiophene)/Tungsten trioxide composite was prepared by an in situ chemical oxidative polymerization of monomer in 1-butyl-3 methylimidazoliumtetrafluoroborate [21]. Then, a Fourier transform infrared (FTIR) spectrum of the PEDOT:WO_3 was obtained by using a Thermo Scientific Nicolet 6700 FT-IR system recorded between 400 and 4000 cm^{-1} with a 4 cm^{-1} resolution. The chemically synthesized PEDOT:WO_3 was dissolved in *N*-methyl pyrrolidine, and spin coated on the chemically cleaned Si substrate at 6000 rpm for 60 s. The thickness of the hybrid film was measured to be 90 nm by a profilometer. Terminally, a circular top metal contact with a 55 nm thickness, was obtained by gold (Au) evaporation at about 3×10^{-6} Torr using a high vacuum metallization system (NANOVAK NVTS400). Finally, the Au/PEDOT:WO_3/p-Si devices were fabricated. Then, the current–voltage and capacitance–voltage measurements of the fabricated devices were accomplished by employing a computer-controlled HP 4140B picoammeter and an HP 4980A LCR meter, respectively. The *I–V* characteristics of one of the fabricated diodes have been performed in the temperature range of 240–320 K, by using a homemade liquid nitrogen cryostat. Dielectric measurements of the PEDOT:WO_3 were carried out by using a computer-interfaced impedance analyzer (Keysight, Agilent/HP 4284A Precision LCR Meter) in the frequency range of 20 Hz to 1 MHz. An input signal of ~ 10 mV was applied to the sample during the measurements.

3 Results and discussion

3.1 Structural, optical and dielectric properties of the PEDOT:WO_3 thin film

3.1.1 FTIR spectrum

FTIR analysis was performed to detect the presence of polymer in the hybrid material. The *FTIR* spectrum of the PEDOT:WO_3 film is given in Fig. 1. When the *FTIR* values of the synthesized PEDOT:WO_3 composite were examined, it was observed that they gave peaks close to each other in other studies in the literature. It appears that typical C–S vibration of the thiophene ring is at 845 and 981 cm^{-1} [22]. The bands at 1105 cm^{-1} and 1213 cm^{-1} area point to the characteristic of the ethylenedioxy group [23]. The peaks at 1359, 1490 and 1540 cm^{-1} wavelengths are of C=C and C–C stretching vibrations in the thiophene ring, respectively

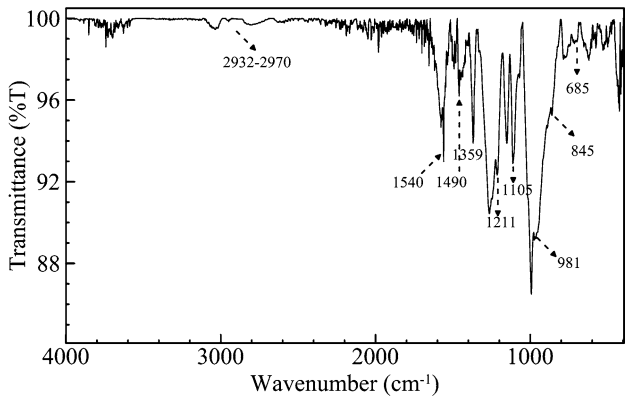

Fig. 1 FTIR spectrum of the PEDOT:WO_3 hybrid film

[23]. The peak at around 623 cm^{-1} is typical of the W–O bond stretching mode [24]. The peaks at around 685 and 1083 cm^{-1} were attributed the vibration of the C–S bond because of stretching of the ethylenedioxy group [25]. The IR bands in the range of 1400–400 cm^{-1} can also belong to the fundamental vibrations of W=O, W–O and W–O–W bonds [26]. The peak at around 2932 or 2970 cm^{-1} was ascribed to the (–OH) stretching vibration of water molecules structurally bound to the WO_3 matrix [17, 27].

3.1.2 AFM analysis

Atomic force microscopy (*AFM*) analysis was performed to measure the roughness profile of the PEDOT:WO_3 film on the chemically cleaned p-Si substrate under non-contact mode (10×10 μm^2 scan size) shown in Fig. 2. Uniformly organized globular structure can be seen in the *AFM* image. From the *AFM* analysis, root-mean-square was found to be 10.49 nm.

3.1.3 UV–Vis spectrum

The optical absorption data of the PEDOT:WO_3 was recorded at room temperature with unpolarized light at normal incidence wavelength in the range of 290–1100 nm using a double beam spectrometer (Fig. 3). The accurate information regarding band gap of PEDOT:WO_3 is essential for various practical applications. The absorption band gap of the PEDOT:WO_3 is determined from the absorbance spectra data and Tauc relation. This relation can be expressed as follows; [28–30];

$$(\alpha h\upsilon)^{\frac{1}{n}} = K\left(h\upsilon - E_g\right) \quad (1)$$

where K is a constant depended on the transition probability and given by the $K = A/d$, d is the film thickness and A is the optical absorbance, n is a constant related to the

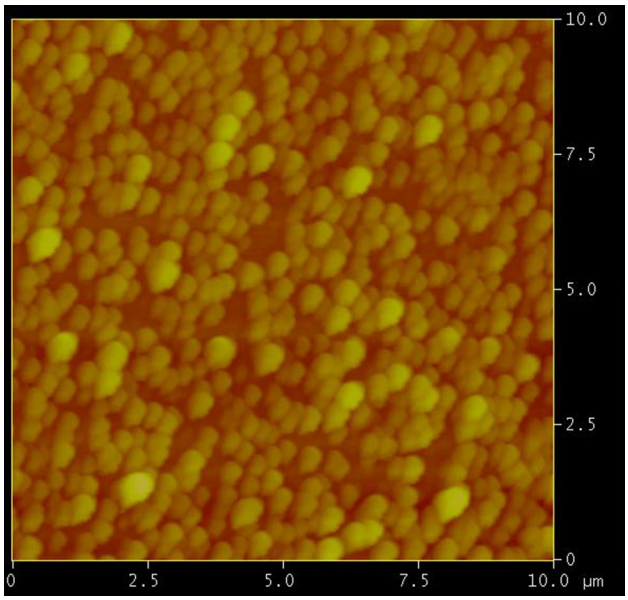

Fig. 2 *AFM* micrograph of the PEDOT:WO_3 film on the chemically cleaned p-Si substrate

distribution of the density states and can be taken 1/2 for direct allowed transitions, $h\nu$ and E_g are the photon energy and the optical band gap energy, respectively.

The corresponding direct optical band gap of the PEDOT:WO_3 was determined using the functional dependence of $(\alpha h\nu)^2$ versus $(h\nu)$ inset in Fig. 3. The direct band gap value of PEDOT:WO_3 was derived by the extrapolating the straight line of this graph at $h\nu = 0$ and it was found to be 2.066 eV and the band around 600 nm is assigned to π–π^* electron transitions in thiophene ring.

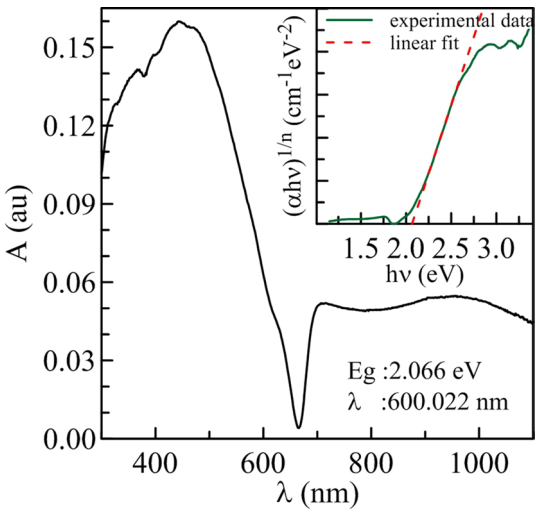

Fig. 3 The absorbance spectra of the PEDOT:WO_3. The inset shows the plots of $(\alpha h\nu)^2$ versus $h\nu$ plot for the PEDOT:WO_3

3.1.4 Dielectric and conductivity properties of the PEDOT:WO_3 thin film

The complex dielectric permittivity, the dielectric loss and the complex conductivity of the PEDOT:WO_3 were experimentally measured and fitted by Eqs. (2) and (3) at room temperature. The analysis details could be found in the literature [31, 32]. The reel (ε′) part and the imaginary (ε″) part of the dielectric permittivity were calculated by following equations;

$$\varepsilon' = \varepsilon_\infty + \frac{\Delta\varepsilon(1 + x^\alpha \cos(\alpha\pi/2))}{1 + 2x^\alpha \cos(\alpha\pi/2) + x^{2\alpha}} \quad (2)$$

$$\varepsilon'' = \Delta\varepsilon \frac{x^\alpha \sin(\alpha\pi/2)}{1 + 2x^\alpha \cos(\alpha\pi/2) + x^{2\alpha}} \quad (3)$$

$$\Delta\varepsilon = \varepsilon_s - \varepsilon_\infty \quad (4)$$

here, ε_∞ is the dynamic dielectric constant as x approaches ∞, ε_s is the static dielectric constant as x approaches 0, ω is the angular frequency of the applied field ($x = \omega\tau$), τ is the average Debye relaxation time, and α is the distribution exponent of the material sample, which has a value between 0 and 1 [31]. The experimental and calculated results were presented in Table 1. The impedance data were further transformed into the dielectric parameters such as ε′, ε″, and conductivity σ.

As shown in Fig. 4, the graph of the real part of the dielectric permittivity indicates two distinct regions of variation. In the first region where is lower than the frequency of 50 kHz, the ε′ exhibits strong frequency dependence. The dielectric constant decreases with increasing frequency. In the second region where is greater than 50 kHz, the real part of the ε′ seems to be almost constant in the lowest value, as the ε″.

The high value of dielectric permittivity observed in the low-frequency region ($f < 50$ kHz) is attributed to the accumulation of space charge [33] due to the polarization effect. The real part of dielectric permittivity decreases with the increase of frequency due to the mobile ions are not able to orient to the high periodic reversal of the applied field. Hence the polarization ability of the structure decreases with increasing frequency. Also, the accumulation of the space charge is also blocked due to the fast switching of the applied field's polarity [34]. In the high-frequency region ($f > 50$ kHz), the low value of the real part of permittivity may be due to the weakening of ion interaction in the transient dipoles [34] in the dc conduction.

At room temperature ε' and ε'' values of the dielectric permittivity of the PEDOT:WO_3 were measured in frequency of 1 MHz as 181 and 353 respectively. At 20 Hz frequency level, these values were measured as, 38,645 and 9,167,750 respectively. The characteristics show that the effect of the polarization is very large in the region of low frequencies. In the high-frequency region, both ε' and ε" decrease.

The ionic conductivity of the PEDOT:WO_3 is in the range of 0.012, and 0.023 Sm^{-1} can be considered high which is not surprising because the electrons of a pure polymer are bonded firmly to the molecule and the polymer has no free moving ion. However, the polymer network and crystallinity

Table 1 Experimental and analytical solution results of dielectric measurement of the PEDOT:WO_3

ε′					ε″		
ε_∞	Δε (×10^5)	τ_ε' (μs)	τ_M (μs)	α	Δε (×10^5)	τ_ε' (μs)	α
3	2.60	0.28	0.187	0.49	749.9	0.07	0.955

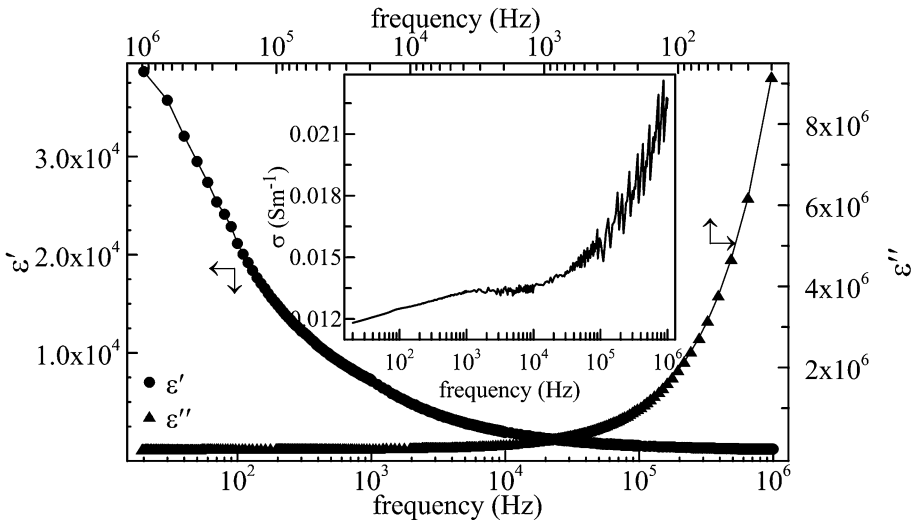

Fig. 4 The real (filled circle) and the imaginary (filled triangle) parts of the permittivity according to frequency. The inset shows the real part of the complex conductivity versus frequency

are substantially affecting the mobility of the ions [35, 36]. On the other hand in the alternative conductivity graph in the inset of Fig. 4, three regions depending upon the frequency are observed. In the first region, which is the low frequency region, there is an evident rise in the conductivity with an increase of the frequency due to the polarization. In this region, the ions jump from one site to another in a faster rate but the relaxation time improves because of the long-range ion transport. The second, intermediate frequency region is called the dc conductivity plateau, which is the frequency independent and nearly constant for the PEDOT:WO_3. This almost constant value in the intermediate frequency region is understandable about the long-range conduction of the charge carriers. At the third, high-frequency region sourced by ac conductivity originated from two opponent short range ion transport (hopping) processes. One of them is unsuccessful, and the other is a successful hopping procedure.

One of the crucial parameters is the relaxation time (τ), which informs about the ion dynamics of the polymer. The relaxation time is inversely proportional to the conductivity. While the relaxation time is decreased the conductivity is improved. In here the low values of τ and α are supporting the relatively high conductivity of PEDOT:WO_3 and it points the structure is the ionic type.

3.2 Electrical properties of the Au/PEDOT:WO_3/p-Si hybrid devices

3.2.1 The current–voltage characteristics of Au/PEDOT:WO_3/p-Si hybrid devices

The dependence of the semi-logarithmic forward and reverse currents on the applied voltage of the 10 Au/PEDOT:WO_3/p-Si devices are shown in Fig. 5, at room temperature. As can be seen from Fig. 5, the *I–V* characteristics of these devices demonstrate rectifying behavior. This behavior can be ascribed to the formation of a potential barrier between the thin film and Si substrate. The *I–V* characteristics of an ideal diode are given by thermionic emission theory [37]. For bias voltage $V \geq 3kT/q$, the conventional diode equation is

$$I = I_o \exp\left(\frac{qV}{nkT}\right), \tag{5}$$

with the saturation current

$$I_o = AA^*T^2 \exp\left(-\frac{q\phi_b}{kT}\right) \tag{6}$$

where q is the electron charge, k is Boltzmann's constant, n is the ideality factor which introduced to account for the departures from thermionic emission theory, A is the geometrical area of the diode, A^* is the effective Richardson

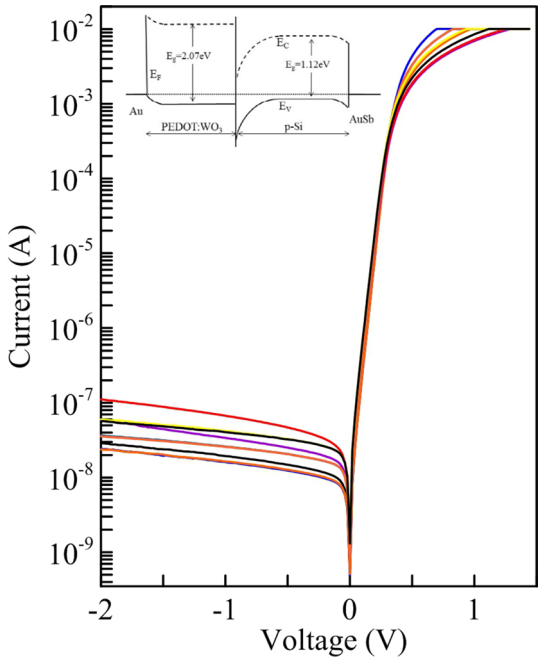

Fig. 5 The plot of current–voltage characteristics of the 10 devices. The energy-level band diagram of the Au/PEDOT:WO_3/p-Si device is shown in the inset

Table 2 The diode parameters obtained from *I–V* measurements of the Au/PEDOT:WO_3/p-Si hybrid devices

Diodes	n	Φ_b $^{(I-V)}$ (eV)	I_0 (A)
D1	1.091	0.741	8.37×10^{-9}
D2	1.084	0.746	6.85×10^{-9}
D3	1.101	0.744	7.51×10^{-9}
D4	1.191	0.719	1.96×10^{-8}
D5	1.134	0.723	1.64×10^{-8}
D6	1.110	0.739	8.88×10^{-9}
D7	1.137	0.724	1.63×10^{-8}
D8	1.127	0.725	1.51×10^{-8}
D9	1.170	0.713	2.45×10^{-8}
D10	1.160	0.714	2.34×10^{-8}
Average	1.131	0.729	1.50×10^{-8}
σ	0.033	0.012	6.20×10^{-9}

constant and equals 32 $Acm^{-2}K^{-2}$ for p-type Si semiconductor, T is the absolute temperature, Φ_b is the effective barrier height. The barrier height and ideality factor values of these devices are calculated from the intercept and slope of the line which is matched to the linear regions of the *I-V* graphs according to the thermionic emission theory and the obtained data were listed in Table 2.

As can be seen from Table 2, the barrier height values for the devices varied from 0.713 to 0.746 eV, and the ideality factor n ranged from 1.084 to 1.191. It is shown

from these results that the parameters of devices vary from diode to diode even if they are almost identically prepared. The barrier height ($\Phi_b^{(I-V)}$) and the ideality factor values of the Au/WO_3:PEDOT/p-Si hybrid devices are given as 0.729 ± 0.012 eV and 1.131 ± 0.033, respectively. The ideality factor of the devices is greater than one. This can be attributed to the interface states and the voltage drop across the interfacial layer containing the native oxide and the composite film [38–40]. Moreover, the barrier height value is significantly greater than the conventional Au/p-Si Schottky diode with the barrier height [38] of 0.34 eV. This enhancement in barrier height can be attributed to the effect of the composite thin film by influencing the space-charge region of the p-Si substrate [39, 40].

Tahir et al. [41] were fabricated PTCDA/PEDOT: PSS based Schottky diodes on the p-Si substrates with ideality factor 3.5 and barrier height 0.81 eV. The thickness of deposited by using spin coating PEDOT:PSS film was 20 nm on the p-Si and annealed in a nitrogen ambient. Martinez et al. [42] reported that the barrier height and the ideality factor of the PEDOT:PSS/n-Si Schottky diode were 0.58 eV and 7.2 respectively. The value of the ideality factor is used to conceive the electronic transport process in Schottky diodes. The ideality factor of the fabricated devices in our study is smaller than the current studies [41, 42]. The differences in the characteristic parameters can be explained due to the variety of the properties of the inorganic semiconductor and the material used as the interface, and the grown techniques and surface cleaning processes. For the Au/PEDOT:WO_3/p-Si devices, the rectification ratio obtained from the ratio of forward and reverse bias current values at ± 1.0 V applied voltage was in the order of magnitude 10^5.

Electrical properties of the contact between the Schottky metal and the WO_3:PEDOT on Si and glass substrate revealed by the transfer length method (TLM) [43]. Specific contact resistance ρ_c and the contact resistance R_c were derived from the *I-V* data of the measured total resistance versus gap spacing by TLM (figure not shown here). The least squares method was used to obtain the intercepts needed to calculate the contact resistance. These values strongly depend on the substrate. R_c and ρ_c values were found to be 24.682×10^9 Ωcm^2, 2559.167 Ωcm^2 and 5.998×10^6 Ωcm^2, 0.0626 Ωcm^2 on glass and Si substrate, respectively.

3.2.2 The capacitance–voltage characteristics of the Au/PEDOT:WO_3/p-Si hybrid devices

The barrier height values of the fabricated devices can be also obtained from the reverse bias *C–V* curves. The *C–V* measurements are made at a sufficiently high frequency of 1 MHz, in which the charges in the interface states cannot follow the alternating voltage signal (ac). At high frequencies, the time constant is too long to allow the charges capture and release in the states in response to an applied ac voltage. The depletion layer capacitance of a rectifying contact fabricated on a p-type semiconductor is given by [38]

$$\frac{1}{C^2} = \frac{2\left(V_{bi} + V_r - \frac{kT}{q}\right)}{q\varepsilon_o\varepsilon_s A^2 N_a} \tag{7}$$

where V_{bi} is the built-in voltage, V_r is the reverse bias voltage, N_a is the acceptor concentration, ε_o is the electric constant of vacuum, ε_s is the static dielectric constant which equals to 11.9 for the Si and other symbols with their usual meaning. The voltage axis-intercept of C^{-2} versus V plot yields V_o. The V_o is related to the built-in voltage by equation $V_{bi} = V_o + kT/q$. The N_a is associated with the slope of C^{-2} versus V curve and obtained from the expression $N_a = 2/q\varepsilon_o\varepsilon_s A^2(1/(d(C^{-2})/dV)$. The barrier height obtained from *C–V* measurement which is given by equation $\Phi_b^{(C-V)} = (V_{bi} + V_p)$, where V_p is the difference between the Fermi level and the top of the valence band in the neutral region of the p-Si and is expressed by $V_p = (kT/q)\ \ln(N_v/N_a)$. The density of states in the valence band is given by $N_v = 2\ (2\pi m^* kT/h^2)^{3/2}$ and is equal to 2.65×10^{19} cm^{-3} [38] for the Si at room temperature. Figure 6 demonstrates the reverse bias C^{-2}–*V* plot of the 10 Au/PEDOT:WO_3/p-Si hybrid devices for 1 MHz and at room temperature. The barrier height values obtained from individual curves were listed in Table 3.

As can be seen from Table 3, the barrier height value of the Au/PEDOT:WO_3/p-Si hybrid devices was given as 0.817 ± 0.011 eV. When the values of the barrier height deduced from the *I–V* and *C–V* data are compared, it is seen

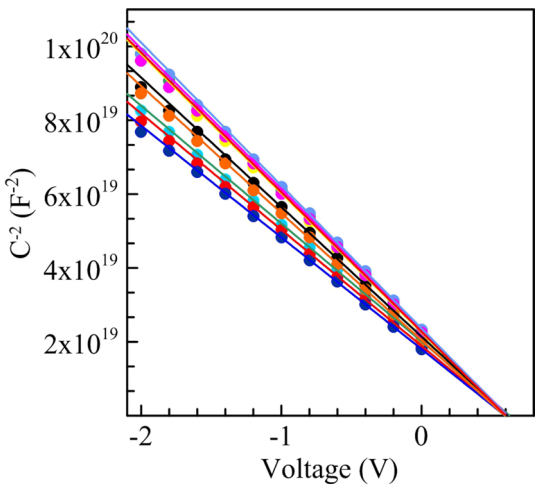

Fig. 6 The plot of C^{-2}–*V* characteristics of the 10 Au/PEDOT:WO_3/p-Si hybrid devices

Table 3 The diode parameters calculated from the *C–V* measurements of the Au/PEDOT:WO_3/p-Si devices

Diodes	N_a ($\times 10^{15}$ cm^3)	V_{bi} (eV)	V_p (eV)	Φ_b $^{(C-V)}$ (eV)
D1	8.084	0.630	0.209	0.839
D2	8.213	0.602	0.209	0.811
D3	8.539	0.597	0.208	0.804
D4	6.784	0.614	0.214	0.828
D5	6.844	0.597	0.214	0.811
D6	7.005	0.595	0.213	0.808
D7	7.381	0.614	0.212	0.825
D8	7.513	0.595	0.211	0.806
D9	6.667	0.610	0.214	0.824
D10	6.817	0.600	0.214	0.814
Average	7.385	0.605	0.212	0.817
σ	0.645	0.011	0.002	0.011

that the barrier height values obtained from the *C–V* data are higher than those deduced of the *I–V* data. The discrepancy between the obtained barrier height values can be attributed to the diversity of nature of *I–V* and *C–V* measurement methods.

3.2.3 The temperature dependent current–voltage characteristics of the Au/PEDOT:WO_3/p-Si hybrid device

In the description of the current transmission mechanism in the hybrid devices, only the *I–V* measurements at room temperature are not sufficient [40, 44–46]. Figure 6 reveals the *I–V* curves of one of the Au/PEDOT:WO_3/p-Si hybrid devices in the temperatures ranging from 240 to 320 K.

The barrier height and ideality factor values of the device were calculated from the intercepts and the slopes of the linear regions of the forward-bias *lnI–V* plots according to the TET at each temperature, respectively, and the obtained values were given in Table 4.

As seen from Table 4, the values of the barrier height and the ideality factor were changed from 0.680 eV and 1.444 at 240 K to 0.726 eV and 1.180 at 320 K, respectively. The values of the ideality factor decrease while the values of the barrier height increase with increasing temperature. Such a variation of the diode parameters can be explained by the non-homogeneity of the barrier height in the hybrid film/inorganic semiconductor interface as in the metal/inorganic semiconductor structures [39, 44, 45, 47–49]. The inhomogeneity of the barrier height may be caused by the change in thickness and composition of the interface layer, the presence of disorder regions in the film, the uniformity of the interface carriers, the locally defective areas [47].

Also, the obtained temperature-dependent barrier height values of Au/PEDOT:WO_3/p-Si hybrid device could be

Table 4 The diode parameters obtained from the *I–V* curves in the temperature range of 240–320 K for one of the Au/PEDOT:WO_3/p-Si hybrid devices

T (K)	n	Φ_b (eV) (forward bias)	I_0 (A)	Φ_b (eV) (reverse bias)	β (experimental)
240	1.444	0.680	7.64×10^{-11}	0.498	2.637×10^{-6}
250	1.385	0.694	1.69×10^{-10}	0.517	2.547×10^{-6}
260	1.357	0.702	4.36×10^{-10}	0.540	2.549×10^{-6}
270	1.319	0.710	1.04×10^{-9}	0.560	2.576×10^{-6}
280	1.281	0.718	2.35×10^{-9}	0.574	2.592×10^{-6}
290	1.260	0.717	7.57×10^{-9}	0.623	3.814×10^{-6}
300	1.220	0.725	1.52×10^{-8}	0.619	3.096×10^{-6}
310	1.228	0.724	4.25×10^{-8}	0.639	3.023×10^{-6}
320	1.180	0.726	6.11×10^{-8}	0.645	2.770×10^{-6}

evaluate with the model of Werner and Güttler [49]. According to this model; at thermodynamic equilibrium (V = 0), the temperature dependence of barrier height can be described by the following equation [49];

$$\Phi_b = \bar{\Phi}_{b0} - \frac{q\sigma_{s0}^2}{2kT} \tag{8}$$

where Φ_{b0} and σ_{s0} are the Gaussian parameters of the barrier height distribution. As can be seen from Fig. 7, the Φ_b obey the double Gaussian distribution with two linear regions. The similar results are also given in Refs. [4, 15, 50, 51] related to heterojunction and Schottky barrier diodes, which attribute the Gaussian distrubition of the Φ_b values to inhomogeneity between metal–semiconductor or semiconductor–semiconductor contacts [50].

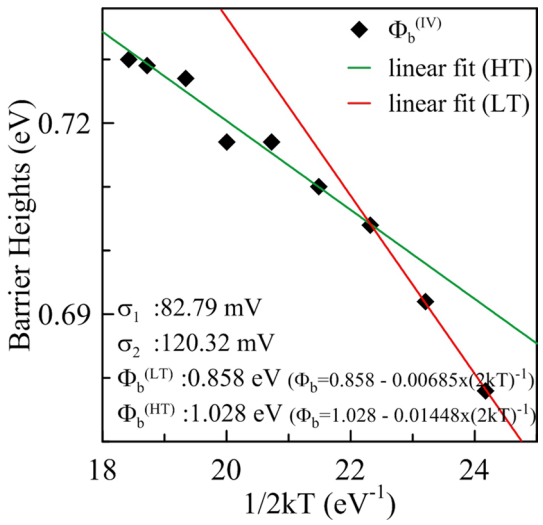

Fig. 7 The Φ_b versus $(2kT)^{-1}$ plot of the Au/PEDOT:WO_3/p-Si hybrid device

The intercepts and slopes of straight lines in Fig. 7 give two sets of values of Φ_{b0} and σ_{s0} which are 0.858 eV and 82.79 meV in the temperature range of 260–320 K [High Temperature Region (HT)], and 1.028 eV and 120.32 mV in the temperature range of 240–260 K [Low Temperature Region (LT)], respectively. The above observations indicate the presence of the double Gaussian distribution of barrier height and the obtained values of σ_{s0} are not low compared to the mean value of Φ_{b0}. Higer values of the standard deviation are usually an indication of large degree of the barrier inhomogeneities at the interface.

Alternatively, the temperature dependence of the barrier height and the ideality factor can also be evaluated according to the thermionic field emission theory. If the current transport through the Schottky junction is controlled by the thermionic field emission, the characteristic tunneling energy and ideality factor are defined as [52];

$$E_{00} = \frac{h}{4\pi}\left(\frac{N_a}{m_h^* \varepsilon_s}\right)^{\frac{1}{2}} \tag{9}$$

and

$$n_{tun} = \frac{E_{00}}{kT} coth\left(\frac{E_{00}}{kT}\right) = E_0/kT \tag{10}$$

where N_a is the acceptor concentration and was found as 1.150×10^{16} cm^{-3} from C–V for the p-Si, $m_h^* = 0.55\ m_0$ [53], and $\varepsilon_s = 11.8\varepsilon_0$, E_{00} as obtained to be 0.8 meV. Figure 8 demonstrates the theoretical temperature dependence of ideality factor estimated for the case when the current through Schottky junction is dominated by the TFE. The solid lines in Fig. 8 were obtained via Eqs. (9, 10) to the experimental temperature dependence values of the ideality factor for the different values of the characteristic tunneling energy. The symbols in Fig. 8 represent the temperature dependence values of the ideality factor determined from the I–V curves in Fig. 9. As can be seen from the figure, the temperature dependence of the ideality factor is in agreement with $E_{00} = 30$ meV. This value of the characteristic tunneling energy is much higher than that of the determined from TFE theory. Thus, it is clear that TFE is not responsible for the current transport in the SBD across the temperature range used here.

Double logarithmic I–V characteristics of one of the Au/PEDOT:WO_3/p-Si hybrid devices is shown in Fig. 10. It is seen that there are three different linear regions from the examination of the graphs. The double logarithmic forward bias I–V characteristics indicate that the current complies with the power law ($I\ \alpha\ V^{m+1}$).

The slope of log–log graphics for the first and third regions is smaller than 2, while the slopes in the second region (0.1–0.3 V) are higher than 2. It is clear from the above observation that the I–V characteristics in the voltage range of 0.1–0.3 V are predominantly controlled by the transmission properties of the composite material. If the slope is greater than 2, it means that the current through the device is limited by the space charge of traps having an exponential distribution in the band gap of the composite

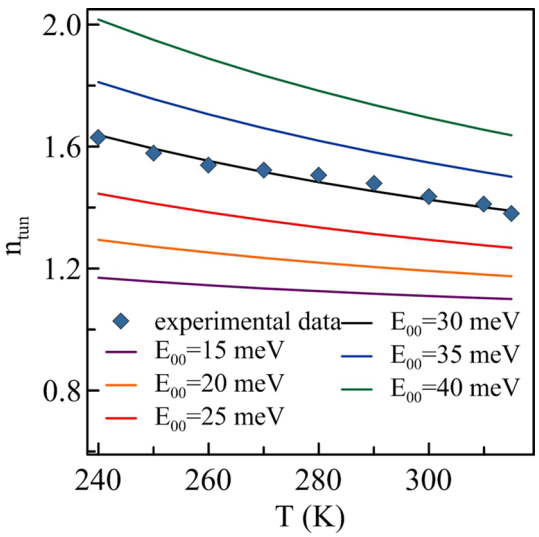

Fig. 8 The plot of $n(T)$ versus T (K) of one of the Au/PEDOT:WO_3/p-Si hybrid devices

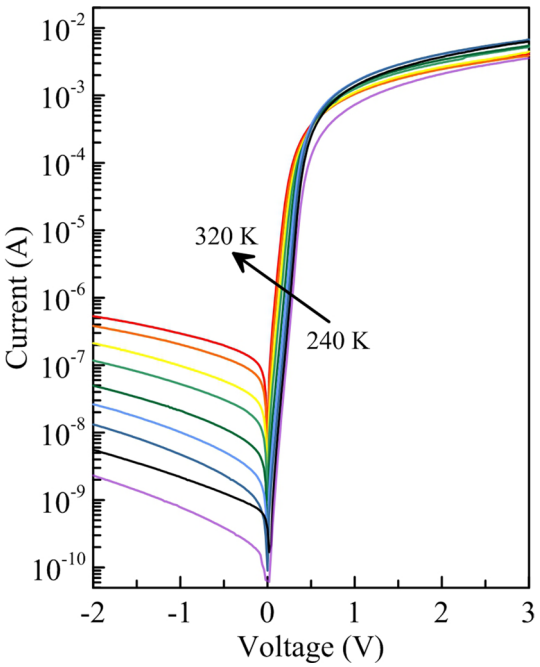

Fig. 9 The I–V curves of one of the Au/PEDOT:WO_3/p-Si hybrid devices in the temperature range of 240–320 K

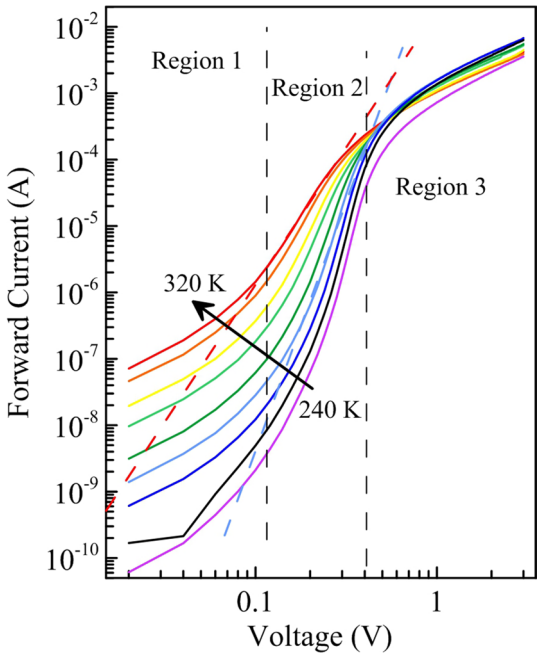

Fig. 10 The forward bias *logI–logV* plot of one of the Au/PEDOT:WO_3/p-Si hybrid devices at different temperatures

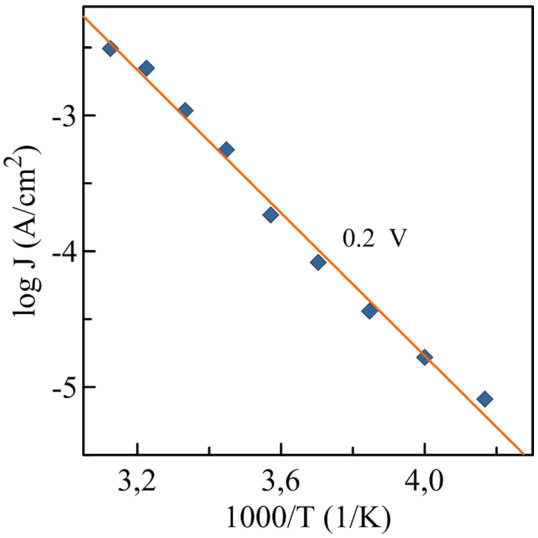

Fig. 11 The plot of forward bias *log (J)* versus *1000/T* at 0.2 V. The solid line indicates the fit to experimental data

layer [54]. The current density for this type of conduction is given by [54, 55]

$$J = \frac{q\mu N_v}{d^{2m+1}}\left(\frac{\varepsilon\varepsilon_o}{qN_t}\right)^m V^{m+1} \tag{11}$$

where μ is mobility of holes in the hybrid film, N_v is the effective density of states in the valence band of the hybrid film which equals to $N_v = 10^{21}$ cm^{-3} [39], ε is the permittivity of the hybrid thin film and is taken as 3.0 [56], ε_o is the permittivity of free space, N_t is the total concentration of traps. As seen from Fig. 10, the value of V_c voltage was found to be 0.45 V from the intersection point of the straights that were fitted to the second regions. The trap concentration for the PEDOT:WO_3 composite film was obtained to be 1.57×10^{16} cm^{-3} with the help of $V_c = {qN_t d^2}/{2\varepsilon\varepsilon_o}$ [56]. In order to determine the carrier mobility in the composite layer, the *logJ* graph is plotted as a function of the inverse of the temperature by determining the current values at a given voltage from the double logarithmic *I–V* curves at different temperatures. Figure 11 reveals the variation of *log (J)* with *1000/T* in the SCLC region at 0.2 V, which gives a straight line. The intercept on the y-axis in the *log (J)* versus *1000/T* plot is given by

$$\log J = log\left(\frac{q\mu N_v V}{d}\right). \tag{12}$$

The value of μ for the PEDOT:WO_3 composite film were obtained as 1.80×10^{-5} cm^2/Vs from the intercept of the curve fitted to the experimental data in Fig. 11. While the mobility value of the hybrid film can be compared to the mobility of some conducting polymers in the literature [40, 57], its value is smaller than that given for the other conductive polymer [58].

In order to determine the electrical properties of the fabricated device, the reverse bias *I–V* characteristics can also be used. Figure 9 reveals that the reverse current of one of the Au/PEDOT:WO_3/p-Si devices in the temperature range 240–320 K increases with increasing bias, but not saturated. As the applied voltage increases, the different mechanisms for the leakage current can occur and become effective. The plot of ln I_R versus $V_R^{1/2}$ for one of the Au/PEDOT:WO_3/p-Si hybrid devices is exhibited in Fig. 12 at different temperatures.

The reverse current conduction of the Au/PEDOT:WO_3/p-Si hybrid device was investigated based on the Schottky emission (SE) and Poole–Frenkel emission (PFE) mechanisms. The PFE and the SE currents as a function of the applied voltage can be stated as [38, 59]

$$I_R = I_o \exp\left(\beta_{PF} V^{1/2}/kTd^{1/2}\right) \tag{13}$$

where I_o is the reverse saturation current, d is the hybrid film thickness, β_{PF} and β_S are the PFE and the SE field-lowering coefficients, respectively, and other symbols their usual meanings. The theoretical values for β_{PF} and β_S are given by

$$\beta_{PF} = 2\beta_S = \left(\frac{q^3}{\pi\varepsilon_o\varepsilon_s}\right)^{1/2}. \tag{14}$$

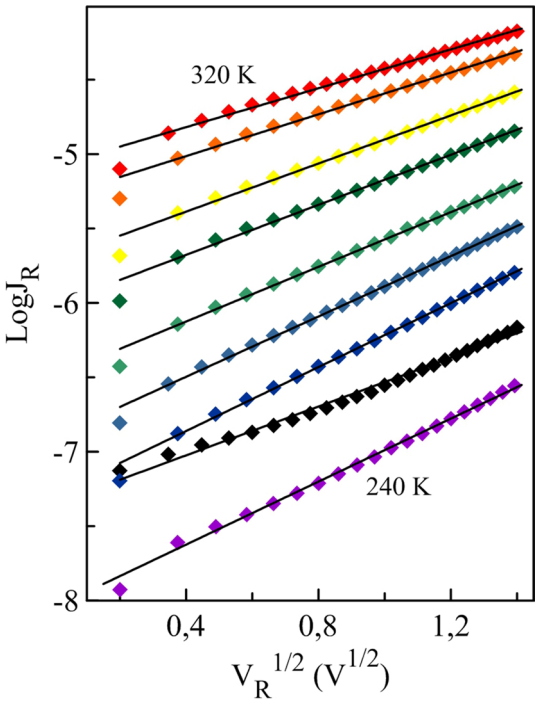

Fig. 12 The plot of $log(J_R)$ versus $V_R^{1/2}$ for one of the Au/PEDOT:WO_3/p-Si hybrid devices. The solid lines indicate the fit to experimental data

Using by Eq. 14, the theoretical values of field-lowering coefficients for the Au/PEDOT:WO_3/p-Si device were obtained as $\beta_{PF}= 2.20\times10^{-5}$ $eVm^{1/2}V^{-1/2}$ and $\beta_S= 1.10\times10^{-5}$ $eVm^{1/2}V^{-1/2}$. The slopes determined from the fit to the data (Fig. 9) for the Au/PEDOT:WO_3/p-Si device were 1.51×10^{-5}, 1.66×10^{-5}, 1.53×10^{-5}, 1.44×10^{-5} and 1.24×10^{-5} $eVm^{1/2}V^{-1/2}$ for 240, 260, 280, 300 and 320 K, respectively. The slopes in the 240–320 K temperature range are closer to the theoretical values of the Schottky emission mechanism. Our experimental results demonstrate that Schottky emission was the dominating current conduction mechanism in the corresponding temperature region.

4 Conclusion

The Au/PEDOT:WO_3/p-Si hybrid devices were fabricated using the PEDOT:WO_3 hybrid film prepared by an in situ chemical oxidative polymerization of monomer in 1-butyl-3-methylimidazoliumtetrafluoroborate on the chemically cleaned p-Si substrate. The bandgap energy of PEDOT:WO_3 thin film was determined as 2.07 eV from UV–Vis spectrum. The *I–V* characteristics of the Au/PEDOT:WO_3/p-Si hybrid device have depicted excellent rectifying characteristics similar to metal-Si Schottky diode.

The barrier height and ideality factor values of the Au/PEDOT:WO_3/p-Si devices were estimated as 0.729 ± 0.012 eV and 1.131 ± 0.033 from the forward bias *I–V* plots, respectively. The determined barrier height value is significantly higher than the conventional Au/p-Si Schottky diode with the barrier height of 0.34 eV. The fabricated devices showed a high barrier height due to the effect of hybride interface layer used and in turn a large rectification ratio (10^5 at ±1 V). Then, the barrier height value of the Au/PEDOT:WO_3/p-Si hybrid devices was determined as 0.817 ± 0.011 eV from the C^{-2}–*V* plots. When the values of the barrier height deduced from *I–V* and *C–V* data are compared, it is seen that the barrier height values obtained from the *C–V* data are higher than those deduced of the *I–V* data. The discrepancy between the obtained barrier height values can be attributed to the diversity of *I–V* and *C–V* measurement methods. The *I–V* characteristics of the device in the 240–320 K temperature range were also investigated. It was seen that the values of the barrier height and the ideality factor were changed from 0.680 eV and 1.444 at 240 K to 0.726 eV and 1.180 at 320 K, respectively. The values of the ideality factor decrease while the values of the barrier height increase with increasing temperature. Such a temperature dependent behavior of the barrier height and the ideality factor was attributed to the lateral inhomogeneity of the barrier height formed at the organic/inorganic interface. The experimental Φ_b vs. $(2kT)^{-1}$ plot for the Au/PEDOT:WO_3/p-Si hybrid device correspond to two lines instead of a single straight line with transition occurring at 260 K.Therefore, the temperature-dependent of SBH of the Au/PEDOT:WO_3/p-Si hybrid device was interpreted on the basis of two presence of two set Gaussian distributions of barrier heights around mean values.

This temperature dependency of diode parameters was also investigated with the TFE and the characteristic tunneling energy was found to be 30 meV. This value of the characteristic tunneling energy is much higher than that of the determined from TFE theory. Moreover, the space-charge-limited current density model dominated by an exponential distribution of traps at high voltages were used to explain the double-logarithmic forward bias *I–V* characteristics of the hybrid device. The trap concentration for the PEDOT:WO3 composite film was obtained to be 1.57×10^{16} cm^{-3}. The bulk properties of the PEDOT:WO_3 film, which is a reliable and suitable candidate for the electronic devices, were calculated using temperature dependent current–voltage- characteristics of the hybrid device. Furthermore, our experimental results show that the dominant conduction mechanism in the reverse bias region of the device is Schottky emission at the corresponding temperatures.

Acknowledgements The authors would like to acknowledge the Scientific Research Projects Unit of Erciyes University for the financial support of project FYL-2018-8011, Erciyes University Nanotechnology Research Center (ERNAM) and Technology Research and Application Center (TAUM) for the AFM and UV–Vis measurements.

References

1. V. Saxena, B.D. Malhotra, Curr. Appl. Phys. **3**, 293–305 (2003)
2. C.N. Van, K. Potje-Kamloth, J. Phys. D Appl. Phys. **33**, 2230 (2000)
3. A.K. Singh, R. Prakash, RSC Adv. **2**, 5277–5283 (2012)
4. H. Çetin, B. Boyarbay, A. Akkaya, A. Uygun, E. Ayyıldız, Synth. Met. **161**, 2384–2389 (2011)
5. S. Aydoğan, M. Sağlam, A. Türüt, J Phys.-Condens. Mat. **18**, 2665–2676 (2006)
6. H. Sirringhaus, T. Kawase, R. Friend, T. Shimoda, M. Inbasekaran, W. Wu, E. Woo, Science **290**, 2123–2126 (2000)
7. B. Boyarbay, H. Cetin, A. Uygun, E. Ayyildiz, Appl. Phys. A **103**, 89–96 (2011)
8. V.R. Reddy, A. Umapathi, L.D. Rao, Curr. Appl. Phys. **13**, 1604–1610 (2013)
9. H. Peisert, T. Schwieger, J. Auerhammer, M. Knupfer, M. Golden, J. Fink, P. Bressler, M. Mast, J. Appl. Phys. **90**, 466–469 (2001)
10. A. Kumar, J. Brunet, C. Varenne, A. Ndiaye, A. Pauly, M. Penza, M. Alvisi, Sens. Actuators, B **210**, 398–407 (2015)
11. M. Raïssi, L. Vignau, E. Cloutet, B. Ratier, Org. Electron. **21**, 86–91 (2015)
12. X. Ma, M. Wang, G. Li, H. Chen, R. Bai, Mater. Chem. Phys. **98**, 241–247 (2006)
13. J. Wei, M. Cheong, N. Nagarajan, I. Zhitomirsky, ECS Trans. **3**, 1–9 (2007)
14. D. Szymanska, I.A. Rutkowska, L. Adamczyk, S. Zoladek, P.J. Kulesza, J. Solid State Electrochem. **14**, 2049–2056 (2010)
15. D. Yıldız, J. Mater. Sci. **29**, 17802–17808 (2018)
16. B. Li, J. Chen, Y. Zhao, D. Yang, D. Ma, Org. Electron. **12**, 974–979 (2011)
17. M. Deepa, A. Srivastava, K. Sood, A. Murugan, J. Electrochem. Soc. **155**, D703–D710 (2008)
18. C. Dulgerbaki, A.U. Oksuz, Adv. Electrode. Mater. **72**, 61–102 (2016)
19. Y.H. Kim, S. Kwon, J.H. Lee, S.M. Park, Y.M. Lee, J.W. Kim, J. Phys. Chem. C **115**, 6599–6604 (2011)
20. W. Kern, *Handbook of Semiconductor Wafer Cleaning Technology* (Noyes Park Ridge, Westwood New Jersey, 1993)
21. C. Dulgerbaki, N. Nohut Maslakci, A.I. Komur, A.U. Oksuz, Electroanal **28**, 1873–1879 (2016)
22. E. Eren, E. Aslan, A.U. Oksuz, Polym. Eng. Sci. **54**, 2632–2640 (2014)
23. S.V. Selvaganesh, J. Mathiyarasu, K. Phani, V. Yegnaraman, Nanoscale Res. Lett. **2**, 546 (2007)
24. C. Dulgerbaki, A.U. Oksuz, Electroanal **26**, 2501–2512 (2014)
25. Y. Lin, L. Huang, L. Chen, J. Zhang, L. Shen, Q. Chen, W. Shi, Sens. Actuators, B **216**, 176–183 (2015)
26. Z.A. Tan, L. Li, C. Cui, Y. Ding, Q. Xu, S. Li, D. Qian, Y. Li, J. Phys. Chem. C **116**, 18626–18632 (2012)
27. V. Chaudhary, A. Kaur, RSC Adv. **5**, 73535–73544 (2015)
28. J. Tauc, *Amorphous and Liquid Semiconductors* (Plenum Press, New York, 1974)
29. J. Tauc, R. Grigorovici, A. Vancu, Physica Status Solidi (b) **15**, 627–637 (1966)
30. E. Güneri, F. Göde, S. Çevik, Thin Solid Films **589**, 578–583 (2015)
31. A. Arya, A. Sharma, J. Mater. Sci. **29**, 17903–17920 (2018)
32. A. Sharma, A.K. Thakur, Ionics **21**, 1561–1575 (2015)
33. J. Gurusiddappa, W. Madhuri, R.P. Suvarna, K.P. Dasan, Indian J. Adv. Chem. Sci. **4**, 14–19 (2016)
34. A. Saroj, R. Singh, S. Chandra, J. Phys. Chem. Solids **75**, 849–857 (2014)
35. S.B. Aziz, O.G. Abdullah, M.A. Rasheed, J. Mater. Sci. **28**, 12873–12884 (2017)
36. A. Jurkane, S. Gaidukov, Preparation and characterization of hot-pressed Li + ion conducting PEO composite electrolytes, in: IOP Conference Series: Materials Science and Engineering, IOP Publishing, pp. 012016, 2016
37. E.H. Rhoderick, R.H. Williams, *Metal-Semiconductor Contacts* (Clarendon Press, Oxford, 1988)
38. S. Sze, *Physics of Semiconductor Devices* (Wiley, New York, 1981)
39. F.E. Jones, C. Daniels-Hafer, B.P. Wood, R.G. Danner, M.C. Lonergan, J. Appl. Phys. **90**, 1001 (2001)
40. M. Kaya, H. Cetin, B. Boyarbay, A. Gok, E. Ayyildiz, J. Phys.-Condens. Mater. **19**, 406205 (2007)
41. M. Tahir, M.H. Sayyad, F. Wahab, F. Aziz, Phys. B **415**, 77–81 (2013)
42. O. Martinez, A.G. Bravo, N.J. Pinto, Macromolecules **42**, 7924–7929 (2009)
43. G.K. Reeves, H.B. Harrison, Electron Device Lett. **3**, 111–113 (1982)
44. A. Akkaya, T. Karaaslan, M. Dede, H. Çetin, E. Ayyıldız, Thin Solid Films **564**, 367–374 (2014)
45. H. Palm, M. Arbes, M. Schulz, Phys. Rev. Lett. **71**, 2224–2227 (1993)
46. V.R. Reddy, Indian J. Phys. **89**, 463–469 (2015)
47. Y.P. Song, R.L. Vanmeirhaeghe, W.H. Laflere, F. Cardon, Solid State Electron. **29**, 633–638 (1986)
48. E. Ayyildiz, H. Cetin, Z.J. Horváth, Appl. Surf. Sci. **252**, 1153–1158 (2005)
49. J.H. Werner, H.H. Guttler, J. Appl. Phys. **69**, 1522–1533 (1991)
50. A. Turut, M. Coşkun, F. Coşkun, O. Polat, Z. Durmuş, M. Çağlar, H. Efeoğlu, J. Alloy. Compd. **782**, 566–575 (2019)
51. B. Boyarbay, H. Cetin, A. Uygun, E. Ayyildiz, Thin Solid Films **518**, 2216–2221 (2010)
52. F.A. Padovani, R. Stratton, Solid State Electron. **9**, 695–707 (1966)
53. S.M. Sze, K.K. Ng, Metal-Semiconductor Contacts, *Environ Sci Eng* (John Wiley & Sons Inc, New Jersey, 2006), p. 832
54. M.A. Lampert, Phys. Rev. **103**, 1648 (1956)
55. M.A. Lampert, R.B. Schilling, Current injection in solids: the regional approximation method. Semicond. Semimet. **6**, 1–96 (1970)
56. M. Yamashita, C. Otani, M. Shimizu, H. Okuzaki, Appl. Phys. Lett. **99**, 213 (2011)
57. L.W. Lim, F. Aziz, F.F. Muhammad, A. Supangat, K. Sulaiman, Synth. Met. **221**, 169–175 (2016)
58. S. Braun, W. Osikowicz, Y. Wang, W.R. Salaneck, Org. Electron. **8**, 14–20 (2007)
59. A.A. Kumar, V.R. Reddy, V. Janardhanam, H.D. Yang, H.J. Yun, C.J. Choi, J. Alloy. Compd. **549**, 18–21 (2013)